Solid Earth
Discussions

Open Access

EGU

1 Syn-thrusting, near-surface flexural-slipping and stress deflection

2 along folded sedimentary layers of the Sant Corneli-Bóixols Anticline

3 (Pyrenees, Spain).

4 Stefano Tavani[1], Pablo Granado[2,3], Pau Arbués[2,3], Amerigo Corradetti[1], Josep A. Muñoz[2,3]

5 [1] DiSTAR, Università degli Studi di Napoli "Federico II", Largo S. Marcellino 10, 80138 Naples, Italy

6 [2] Institut de Recerca Geomodels, Universitat de Barcelona, Martí i Franquès s/n, 08028 Barcelona, Spain

7 [3] Departament de Dinàmica de la Terra i de l'Oceà, Universitat de Barcelona, Martí i Franquès s/n, 08028 Barcelona, Spain

8 *Correspondence to*: Stefano Tavani (stefano.tavani@unina.it)

9 **Abstract.** In the Spanish Pyrenees the Sant Corneli-Bóixols thrust-related anticline displays an outstandingly preserved

10 growth strata sequence. These strata lie on top of a major unconformity exposed at the anticline's forelimb that divides and

11 decouples a lower pre-folding unit from an upper syn-folding one. The former consists of steeply-dipping to overturned

12 strata with widespread bedding-parallel shears indicative of folding by flexural-slip, whereas the syn-folding strata above

13 define a 200-m amplitude S-shaped fold. In the inner and outer sectors of the forelimb, both pre- and syn-folding strata are

14 near-vertical to overturned and the unconformity angle ranges from 10° to 30º. In the central portion of the forelimb, syn-

15 folding layers are shallowly-dipping, whereas the angular unconformity is about 90° and the unconformity surface displays

16 strong S-C shear structures, which provide a top-to-the foreland shear sense. This sheared unconformity is offset by steeply-

17 dipping faults which are at low angles to the underlying layers of the pre-folding unit. Strong shearing along the

18 unconformity surface also occurred in the inner sector of the forelimb with S-C structures providing an opposite, top-to-the

19 hinterland, shear sense. Cross-cutting relationships and shear senses along the pre-folding bedding surfaces and the

20 unconformity indicate that regardless of its orientation, layering in the pre- and syn-folding sequences of the Sant Corneli-

21 Bóixols anticline was continuously sheared. This shearing promoted an intense stress deflection, with the maximum

22 component of the stress tensor remaining at low angles to beds during most of the folding process.

23 1 Introduction

24 Templates used to describe the state of stress of growing regional-scale thrust-related anticlines (e.g. Hancock, 1985; Lisle,

25 1994; Fischer and Wilkerson, 2000; Belayneh and Cosgrove, 2004; Tavani et al., 2015), typically integrate punctual strain

26 data (e.g. Engelder and Geiser, 1980; Laubach, 1989; Lacombe, 2012; Balsamo et al., 2016) and indirect information

27 provided by the large-scale geometry of the structure, such as like curvature or strata thinning/thickening (e.g. Price and

28 Cosgrove, 1990). Widespread documentation of bedding-parallel slip, along with the broad preservation of layer thickness,

29 provide key information to model the distribution of stress in actively growing anticlines. These observations indicate

30 flexural-slip folding in the multilayered portions of reservoir-scale thrust-related folds (e.g. Donath and Parker, 1964;

31 Ramsay; 1967; Tanner, 1987; Suppe, 1983; Fowler, 1996; Erslev and Mayborn, 1997). The assumption/observation of

32 flexural-slipping has important consequences on the stress distribution:

33   - Shearing along numerous bedding surfaces in a wide range of bedding dip, is possible only where the bedding

34   surfaces have a low friction and a low cohesion.

35   - On the other hand, the reactivation of these closely spaced low friction surfaces should prevent the layer-parallel

36   shear to exceed a certain value, which in turn imposes the direction of the maximum component of the stress field

37   to be at low angle to bedding, i.e. at low angle to the shearing surface (Wiltschko et al., 1985; Ohlmacher and

38   Aydin, 1997; Tavani et al., 2015).

39 The process of layer-parallel shearing is, however, discontinuous in time and space, so that it is unclear whether the regional

40 stress reorients only locally or, rather, the layer-parallel slipping is sufficiently dense, both in time and space, to promote the

41 reorientation of the stress in wide - actively folding - areas. Field documentations are in agreement with the second

42 hypothesis, i.e. that shearing along low-friction bedding surfaces promotes deflection of the principal directions of the

43 remote stress field, with the direction of the maximum stress keeping at low angle to layers, so that the maximum stress in

44 active fold and thrust belts maybe not always strictly horizontal. In fact, syn-folding layer-parallel shortening structures are

45 reported in the folded pre-growth strata of many thrust related anticlines (e.g. Tavani et al., 2006; 2012). However, paleo-

46 stress and/or paleo-strain indicators cannot easily and unequivocally constrain the bedding dip values range at which such

47 stress deflection mechanism can operate (e.g. Callot et al., 2010; Beaudoin et al., 2012). In fact, almost all published datasets

48 come uniquely from pre-growth sequences of thrust-related folds. In these cases, deciphering for which bedding dip values a

49 given set of deformation structures are formed (i.e. fractures or slickenlines along a bedding surface) remains difficult, and

50 any assumptions made carry along significant uncertainty.

51   On the other hand, observations made in syn-growth layers of thrust-related anticlines allow to drastically reducing

52 uncertainties related to the timing of deformation (e.g. Shackleton et al, 2005, 2011). As a matter of fact, the study of growth

53 strata sequences are by far the most commonly used approach for understanding the kinematics of fault-related folds in

54 contractional settings (e.g. Suppe et al., 1992; Burbank et al., 1996; Ford et al., 1997; Suppe et al., 1997; Vergés et al., 2002).

55 In contrast with the abundance of detailed geometrical studies (Suppe, 1983; Medwedeff, 1989; Mitra, 1990; Suppe and

56 Medwedeff, 1990; Zapata and Allmendinger, 1996; Poblet et al., 1997; Suppe et al., 1997), few contributions dealing with

57 the dynamics of folding inferred from syn-kinematic layers have been published (e.g. Ford et al., 1997; Nicol and Nathan,

58 2001; Shackleton et al., 2011; Beaudoin et al., 2015), mostly because of the lack of well-preserved and accessible exposures.

59 In this work we have focused on the macro and meso-structures developed within a growth strata wedge and a related major

60 syn-kinematic unconformity exposed at the forelimb of the Sant Corneli-Bóixols anticline. Bedding-parallel shear occurs

61 along pre and syn-kinematic strata, which are oriented obliquely to each other, together with meso-scale faults cutting across

62 strata and the unconformity. Thus, this area provides an excellent, almost unique, field example to observe, describe, and

63 analyse how anisotropies oblique to each other, i.e. layers and unconformity, respond to progressive shortening and related

64 folding in a contractional setting. In addition, the studied area allowed us to determine the threshold dip value at which

65 flexural-slip is of sufficient magnitude to deflect the maximum principal stress direction from the regional stress field.

66 **2 Geological Setting**

67   The Pyrenean Belt is a doubly-vergent orogenic wedge (Fig. 1a) formed during the Late Cretaceous to Miocene

68 subduction of the Iberian lithosphere beneath the Eurasian plate (e.g. Choukroune et al. 1990; Muñoz, 1992; Teixell, 1998).

69 It largely deformed and inverted the Mesozoic extensional basins developed between Iberia and Eurasia during the Mesozoic

70 separation of these two plates (Muñoz, 2002). The Early Cretaceous Organyà basin is one of these basins interposed between

71 the Iberian plate and the exhumed mantle of the Pyrenean rift (e.g. Tugend et al., 2014). Upon convergence and shortening,

72 the Organyà basin was positively inverted and incorporated into the hanging-wall of the Bóixols thrust starting on Late

73 Cretaceous times (e.g. Mencos et al., 2015 and references therein). The positive inversion of the inherited extensional

74 structures occurred under oblique, NNW-SSE oriented, convergence (Tavani et al., 2011), and was responsible for the

75 development of the E-W striking Sant Corneli-Bóixols anticline (Fig. 1a). The location and geometry of this anticline is

76 controlled by the orientation of the Early Cretaceous extensional border fault system of the Organyà basin (e.g. Bond and

77 McClay, 1995; García-Senz, 2002; Mencos et al., 2015).

78   Several detailed studies of the stratigraphy of the Organyà basin were carried out in the last 50 years (e.g. Rosell,

79 1963; Garrido; 1973; Simó, 1986; Berástegui et al., 1990; García-Senz; 2002, Mencos, 2011). The pre-rift Mesozoic

80 stratigraphy is represented by clays and evaporites belonging to the Triassic Keuper facies, followed by Jurassic shallow

81 marine carbonates and deeper water marls. The Early Cretaceous syn-rift megasequence consists of platform carbonates that

82 thicken towards the north and transition laterally (i.e. toward the north) into basinal marls (e.g. García-Senz, 2002). In the

83 hanging-wall of the Bóixols thrust the maximum thickness of the syn-rift megasequence is about 4500m. It thins southwards

84 around the hinge zone of the Sant Corneli-Bóixols anticline across the extensional fault system at the southern margin of the

85 Organyà basin (Lanaja et al., 1987; Berástegui et al., 1990; Arbués et al., 1996; García-Senz, 2002; Muñoz et al., 2010;

86 Mencos et al., 2015). The Upper Cenomanian to Lower Santonian post-rift megasequence consists of carbonates with lesser

87 clastics and can be up to 700m thick (García-Senz, 2002; Mencos, 2011). The syn-orogenic strata are exposed in the leading

88 syncline (i.e. Tremp-Sallent Syncline) of the Sant Corneli-Bóixols anticline (Fig. 1a-b) and include more than 1000m of

89 Upper Santonian to Paleocene deepwater to continental strata that thin abruptly to a few tens of meters northwards, i.e.

90 towards the Sant Corneli-Bóixols anticline (e.g. Arbués et al., 1996; Roma et al. 2011).

91   In the studied area, the syn-orogenic succession can be subdivided into two units (Figs. 1b-c): (1) The lower, Upper

92 Santonian to Campanian, Vallcarga Group (Nagtegaal, 1972) is constituted by a multilayered marine sequence of thin to

93 medium bedded limestones and mudstones. Around the Sant Corneli-Bóixols Anticline the Vallcarga Group was deposited

94 during folding as evidenced by growth geometries at the eastern tip of the Sant Corneli Anticline (Mencos et al., 2015).

95 However, no clear evidences of deposition during the early stages of folding are visible in the studied area and hence it is
96 here geometrically considered as pre-kinematic but within a regional syn-orogenic scenario. (2) The Late Campanian to
97 Maastrichtian Areny Group (Arbués et al., 1996) is unconformably overlying the Vallcarga Group. Its thickness exceeds
98 1000m in the Tremp-Sallent Syncline depocentre (Fig.1a-b) but thins abruptly to a few tens of meters towards the Sant
99 Corneli-Bóixols Anticline so it is considered to have been deposited during folding (i.e. syn-folding). The Areny Group
100 records sedimentation in neritic to deep marine conditions coeval with the inversion and related folding of the Organyà
101 extensional basin. The Areny Group has been divided into four sequences (A1 to A4 from older to younger; Arbués et al.,
102 1996) and broadly includes rudist accumulations and talus marls, sandstones, and re-sedimented equivalent in turbiditic
103 facies. (3) The syn-folding Maastrichtian to Paleocene Tremp Group (Cuevas, 1992) includes continental facies associations
104 which are commonly referred to as the Garumnian facies (Cuevas, 1992). These consist of alluvial and colluvial
105 conglomerates and breccias, passing southwards to alluvial plain and fluvial reddish sandstones and mudstones (e.g. Arbués
106 et al., 1996; Roma et al., 2011).

107   From a structural point of view, the major structures in the studied area are the Bóixols thrust and related splays, the
108 E-W trending Sant Corneli-Bóixols Anticline and the associated Santa Fe Syncline to the north and the Tremp-Sallent
109 Syncline to the south (Fig. 1a). The main ramp of the Bóixols thrust crops out in the studied area, whereas to the west and to
110 the east it remains blind along most of the frontal limb of the Sant Corneli-Bóixols Anticline. In its exposed sector, the
111 Bóixols thrust has Triassic to Upper Cretaceous pre-growth rocks in its hanging-wall and syn-orogenic and syn-folding strata
112 in its footwall (Fig. 1c). A thin sheet of overturned post-rift limestones, mainly the upper Cenomanian ones, defines two
113 thrusts. The lower thrust remains blind beneath the vertical beds of the Garummnian succession at the northern limb of the
114 Sallent Syncline. The upper one on the other hand truncates the Garumnian beds. This upper one is the Bóixols thrust and
115 according to magnetostratigraphic and thermochronological studies it would have been reactivated during Paleogene times
116 (Beamud et al., 2011). The pre-folding beds of the Vallcarga Group in the footwall of the Bóixols thrust are folded into a
117 syncline with overturned strata immediately below the thrust fault. These strata progressively acquire sub-horizontal attitudes
118 in the Tremp-Sallent Syncline to the south (Fig. 1c). Conversely, the unconformably overlying Areny and Tremp Groups
119 display a series of folded structures, namely the Sant Maximí Syncline and the Tremp-Sallent Syncline, with the Remolina
120 Anticline in between. The Remolina Anticline disappears toward the east, where the two synclines join (Fig. 1b). The three
121 folds display a significant eastward plunge (Roma et al., 2011) of 24° with a 72° strike, as derived by the direction normal to
122 the best fit plane of bedding data of the Areny Group (Fig. 1c).

3 Macro- and Meso-structures

124   In the following, we describe the structural assemblages occurring along and around the major unconformity
125 dividing the Areny from the Vallcarga Group, i.e., the lower syn-folding strata from the upper syn-folding strata (Fig. 1d).
126 The macro- and meso-structures are described from north to south in three sub-sections, corresponding to the three limbs of
127 the S-shaped fold that define the Sant Maximí Syncline, the Remolina Anticline, and the Tremp-Sallent Syncline (Fig. 1). We

128 will present and discuss stereoplots of bedding attitude, fault orientations and kinematic indicators from faults. In these
129 stereoplots the plane normal to the structural plunge is also displayed, in order to ease the interpretation of the faults
130 kinematics. For each stereoplot, we also show the two graphs resulting from the removal of plunge first and then of the
131 residual bedding dip (Ramsay, 1967).

132 **3.1 Northern limb**

133 In the inner (northern) limb of the Sant Maximí Syncline, the marls and limestones of the Vallcarga Group are
134 overturned, while the unconformably overlying strata of the Areny Group are steeply south-dipping to near-vertical (Fig. 2).
135 In the northern limb of the syncline, the strata of the Areny Group include siltstones, sandstones, and conglomerates
136 belonging to the A4 sequence; the A1 to A3 sequences are missing (Fig. 2a-b), either because they were never deposited
137 there or because they have been eroded before the deposition of the A4 sequence. Overturned bedding surfaces of the
138 Vallcarga Group display evidence of shearing. Movements along bedding are mostly toward the NW with normal sense of
139 slip in the present overturned bedding orientation (Fig. 2b). Stereoplots show that slickenlines along bedding surfaces of the
140 Vallcarga Group are mostly perpendicular to the local fold axis. The unconformity between the Vallcarga and the Areny
141 Groups has been reactivated as a thrust and displays an intense S-C fabric that affects few meters of the Vallcarga Group
142 (Fig. 2c). Analogously to other S-C tectonites developed in carbonates and at shallow depth (e.g. Tesei et al., 2013; Vitale et
143 al., 2014), the S-C structures found in the first 2-3 m of the Vallcarga Group immediately below the unconformity, formed as
144 consequence of pressure-solution of marly limestones and marls, and thus indicating a ductile to brittle-ductile behaviour of
145 the Vallcarga Group in correspondence of this major fault. Slip directions provided by C, S and C' structures are top-to-the-
146 NW and, similarly to the bedding-parallel slip surfaces, the average slip direction lies along the plunge-normal plane (Fig.
147 2c). The Areny Group conglomerates immediately above the unconformity are not affected by S-C fabric, whereas siltstones
148 occurring few meters above the unconformity are affected by a strong cleavage (Fig. 2d). This cleavage is at high angle to
149 bedding, as seen in the field and as evidenced by the fact that poles to cleavage in the stereoplot occur close to the bedding
150 planes great circles (Fig. 2d). However, cleavage is not strictly bedding-perpendicular. Once bedding dip is restored to the
151 horizontal, the poles to cleavage still lay along the plunge normal-plane and cleavage becomes SE-dipping. These
152 relationships are indicative of a minor top-to-NW shear component during cleavage development.

153 **3.2 Central limb**

154 Immediately to the south of the axial surface of the Sant Maximí Syncline, strata of the Areny Group are shallow dipping to
155 sub-horizontal (Fig. 1c-d). Locally, however, strata of the A4 sequence of the Areny Group are steeply north-dipping and the
156 Sant Maximí Syncline forms a tight structure with a north-dipping to near vertical axial surface. In the hinge zone, the
157 unconformable strata of the Areny Group are separated from the underlying overturned strata of the Vallcarga Group by a
158 sub-horizontal shear zone, which corresponds to the sheared syn-folding unconformity (Fig. 3). In addition, the sheared
159 unconformity is offset by a series of high-angle faults that uplift the southern block (Fig. 3b). Striae along bedding surfaces
160 of the Vallcarga Group indicate top-to-N movements with normal kinematics (Fig. 3b). Striae within the sub-horizontal shear

Solid Earth
Discussions

Open Access

EGU

161 zone indicate top-to-S movement, whereas the high angle faults that offset it have slickenlines lying along the plunge-normal

162 plane and show a top-to-N movement. A few strike-slip slickenlines also occur along high angle faults, and are indicative for

163 left-lateral movements. In other places, the system of high angle reverse faults uplifting the southern limb of the Sant

164 Maximí Syncline displays a top-to-NW movement, including some right-lateral kinematic indicators (Fig. 3c). Looking at

165 the system of high angle faults in natural cross-sections at a larger scale of observation (Fig. 3c), it is evident that these faults

166 are approximately (i.e. angular difference is less than 10°) parallel to the layers of the Vallcarga Group, and that the amount

167 of uplift of the southern block is few tens of metres.

168   The uplifted southern block is well exposed at the Sallent hill (Fig. 4). There, the sub-horizontal rudist-bearing units

169 of the Areny Group A3 sequence sit unconformable on top of the overturned north-dipping strata of the Vallcarga Group

170 (Fig. 4a-b). Slickenlines are consistently found along the bedding surfaces of these strata. As shown in the stereoplots of

171 Figure 4a, most of slickenlines display top-to-N normal kinematics, whereas a few are characterised by strike-slip (both left-

172 and right-lateral) or reverse kinematics. The slickenlines displaying strike-slip and reverse kinematics postdate the top-to-N

173 normal ones. Faults oblique to bedding have been also found in the Vallcarga Group in this area (Fig. 4a). These faults are at

174 low angle with the bedding surface and display normal and, subordinately, reverse kinematics. After bedding dip removal,

175 both bedding-parallel shear surfaces and bedding-oblique faults, show a top-to-NW shear sense. As mentioned above, strata

176 of the rudist-bearing A3 sequence are shallow dipping (Fig. 4a-b) and the unconformity between the Areny and the Vallcarga

177 groups is also sub-horizontal. The unconformity is affected by a pervasive shear fabric (Fig. 4c) with S, C, and C' structures

178 providing a top-to-SSE shear sense. In addition, the sheared unconformity is cross-cut by SSE-dipping and NNW-verging

179 reverse faults (Fig. 4b).

3.3 Southern limb

181   Strata of the Areny Group are overturned to mostly steeply south-dipping to the south of the Remolina Anticline,

182 strata of the Areny Group are overturned to mostly steeply south-dipping (Fig. 5a). These strata are still unconformable on

183 top of the overturned strata of the Vallcarga Group, but the unconformity angle between the two groups becomes

184 significantly reduced down to about 20°. The unconformity preserves its stratigraphic origin and, as opposed to the northern

185 and central limbs of the Sant Maximí syncline, no appreciable evidence of shear occurs (Fig. 5b). Instead, striae along the

186 bedding surfaces of the Areny Group are observed (Fig. 5c). These striae indicate normal top-to-NNW and reverse top-to-

187 NNE movements along north-dipping overturned and steeply south-dipping strata, respectively (Fig. 5c). In both cases, striae

188 lie along the bedding surfaces at the intersection between bedding and the plunge-normal plane (Fig. 5c). Faults at low angle

189 to bedding have the same behaviour as the bedding: south- and north-dipping faults are reverse and normal, respectively,

190 with slickenlines lying at the intersection between the fault and the plunge normal plane (Fig. 5c). Once bedding dip is

191 restored to the horizontal, a top-to-NNW shear sense is provided by both faults and bedding-parallel shear surfaces.

3.4 Structural summary

193   The deformation structures observed along and around the unconformity separating the upper syn-folding strata of

194   the Areny Group from the underlying multilayered limestones and marls of the Vallcarga Group can be summarised as
195   follows:

196   In the Vallcarga Group, many of the E-W striking bedding surfaces of near-vertical to overturned strata have been
197   reactivated as shear surfaces. Most of these bed-parallel shear surfaces exhibit dip-slip kinematics, with only a few beds
198   showing strike-slip movements. After removing the plunge of the structure and then restoring the local bedding to the
199   horizontal, most of the slickenlines measured along the bedding surfaces provide a shear sense ranging from top-to-NW to
200   top-to-N, with an average top-to-NNW movement. Faults are roughly E-W to WSW-ENE striking and show very low cut-off
201   angles to bedding. After removing the fold plunge and the bedding dip, these faults provide the same top-to-NNW shear
202   sense as the bedding-parallel slickenlines. Some faults, which are presently steeply dipping to near vertical, have cut-off
203   angles of ranging from 20° to 40° and after removing plunge and bedding dip show normal kinematics. Still, the shear sense
204   provided by them after bedding dip removal is top-to-NNW. This fault pattern and the illustrated kinematics of bedding
205   surfaces is observed all across the studied thrust-related fold profile, i.e. in the northern, central, and southern limbs.

206   The syn-folding unconformity is characterised by an intense S-C fabric (showing also some C' structures) in the
207   northern limb, and in the sub-horizontal central limb. In both cases, shear direction is roughly NNW-SSE, although some
208   strike-slip movements are occasionally observed. However, the shear sense is opposite in the two limbs, being top-to-NNW
209   in the northern limb (i.e., where the sheared unconformity strikes about E-W and has a near vertical attitude) and top-to-SSE
210   in the central limb (i.e., where the sheared unconformity is offset by the steeply-dipping to near vertical faults surging from
211   the underlying Vallcarga Group). Further to the south, in the southern limb of the Remolina Anticline, the unconformity
212   shows little evidence of deformation.

213   Strata of the Areny Group exposed at the northern limb are affected by an intense cleavage at high angle to bedding.
214   The cleavage-bedding angle is not exactly 90° however, indicating the occurrence of a top-to-NNW bedding-parallel shear
215   component. Slickenlines are observed along the bedding surfaces of the near vertical to overturned strata of the Areny Group
216   exposed at the southern limb of the Remolina Anticline. In this area, some faults at very low angle to bedding occur. For both
217   faults and bedding surfaces, the shear sense measured after removing the plunge and the bedding is roughly top-to-NNW.
218

4 Chronology of deformation stages
220   The syn-folding strata of the Areny Group exposed at the forelimb of the Sant Corneli-Bóixols Anticline are
221   unconformably on top of north-dipping overturned strata of the pre-folding Vallcarga Group. The unconformity between both
222   groups is clearly a syn-folding feature. Its unconformity angle varies across the studied area, and in addition, its surface
223   shows unequivocal evidence of strong shearing with an average NNW-SSE-oriented shear direction. Such shear direction is
224   parallel to the slip directions measured along both faults and bedding surfaces of the Vallcarga and Areny groups. The NNW-
225   SSE direction is not perpendicular to the strike of the hosting anticline tough. This structural relationship reaffirms that the
226   E-W striking Sant Corneli-Bóixols Anticline has developed under an oblique convergence setting where the shortening

Solid Earth
Discussions

Open Access

EGU

227   direction was NNW-SSE (Tavani et al., 2011). In this sense, the observed meso-structures are interpreted as developed

228   during the growth of the Sant Corneli-Bóixols Anticline, and they cannot be attributed to a subsequent tectonic event. The

229   fact that these structures occur in syn-folding strata, also rules out a pre-folding origin. In agreement with this, the observed

230   opposite shear senses along the unconformity surface to the north and to the south of the San Maximí Syncline axial surface

231   have a syn-folding origin. As illustrated in the next section these opposite senses of shear can be used to unravel the

232   kinematic evolution of the unconformity, the unconformity angle itself and therefore that of the Sant Corneli-Bóixols

233   Anticline.

234

5 Modelling the folding of the angular unconformity

236   Guidelines about flexural-folding of angular unconformable sequences where firstly provided by Alonso (1989).

237   These include the progressive variation of the unconformity angle during tilting of pre-unconformity layers, synchronously

238   with progressive shearing along the unconformity surface (Alonso, 1989). Figure 6a illustrates the folding of an

239   unconformable sequence using a kink-band template with synclinal geometry. The position of six key-points undergoing

240   folding is illustrated, where the fixed P_1 point is the origin of our reference system. The simple kink-band construction is

241   used to quantify how the unconformity angle and the amount of shear along the unconformity are modified during folding,

242   where D_0 is the initial dip of layers, U_0 the initial unconformity angle, H_0 the stratigraphic elevation of the unconformity, and

243   L_0 the distance from the origin of an arbitrarily placed pin line (note that the L_0 parameter will disappear from the final

244   equations used here). The X and Y coordinates of the 6 key points and the length of the segments joining them can be

245   expressed as a function of L_0, H_0, U_0, D_0, and D, as provided in figure 6b. In particular, the length of the segment joining

246   points P_5 and P_4 provides the amount of shear (ΔS, considered positive when top-to-the-hinterland), while points P_3 and P_4

247   allow calculating the unconformity angle (U).

248   As folding takes place, the unconformity angle increases and the shear sense along the unconformity is initially top-

249   to-the-hinterland, i.e. in the same sense as the flexural-slip along the pre-unconformity layers. When the pre-unconformity

250   strata become overturned, the unconformity angle continues to increase and the flexural-slip in the pre-unconformity layers

251   continues to be top-to-the-hinterland; instead the shear sense along the unconformity flips and becomes top-to the foreland.

252   Close to the leading syncline, i.e. along the P_2P_3 segment, the incremental shear sense is top-to-the-hinterland, whereas along

253   the P_3P_4 segment it becomes to top-to-the-foreland, despite the cumulative shear sense may continue to be top-to-the-

254   hinterland.

255   The relationship between U, U_0, and D derived in figure 6b, are graphed in figure 6c. The relationships between U

256   on D (blue lines in the figure) for different U_0 values, indicate that:

257   (1) It is possible to develop overturned pre-folding strata and a nearly sub-horizontal unconformity, as observed in

258   the central limb of our study area, (i.e. the unconformity angle is roughly equal to the dip of the pre-unconformity

259   layer) for a wide range of initial unconformity angles (from 30° to 90°).

260   (2) In order to obtain an unconformity angle of less than 20° where the pre-unconformity strata are near vertical, as
261   observed in the northern and southern limbs of the study area, the initial unconformity angle cannot exceed 10-15°.
262 The predicted amount and sense of shear (normalised to H_0) at different tilting stages (i.e. for different D) and for different
263 initial unconformity angles (i.e. U_0) is plotted in red in figure 6c, where positive and negative values indicate top-to-the-
264 hinterland and top-to-the-foreland shear, respectively. For small initial unconformity angles, the unconformity angle and the
265 cumulative top-to-the-hinterland slip along the unconformity increase during folding. This occurs until the dip of pre-growth
266 strata attains a near-vertical attitude. From this point, further folding would imply overturning of strata and the decrease of
267 the cumulative top-to-the hinterland slip, which eventually becomes negative (i.e. top-to-the-foreland sense), while the
268 unconformity angle U exceeds 90° Where the initial unconformity angle is instead close to 90°, progressive folding would
269 imply a short period of top-to-the-foreland shearing along the unconformity, followed by top-to-the hinterland shearing when
270 strata become nearly vertical to overturned. At this point it is important to remark that the progressive and the incremental
271 shear senses do not coincide. The D value at which the cumulative shear passes from top to the hinterland to top-to-the-
272 foreland largely depends on the initial unconformity angle U_0. Conversely, for an initial unconformity angle U_0 between 45°
273 to 90° the incremental shear changes its sign for values of D ranging from 80° to 90°, and almost regardless on U_0, value (the
274 regions where the incremental shear has opposite directions are in white and grey in figure 6c).

275   The absence of any kinematic indicator of top-to-the-hinterland shear in the central limb of the study area, indicates
276 that the initial unconformity angle had to be high at that position, and if any, the initial stage of top-to-the-hinterland shearing
277 was negligible. This can be achieved when the initial unconformity angle is at least 70-75°. This represents a key argument
278 for unravelling the deformation sequence, as structures postdating the top-to-the foreland shearing have to be interpreted as
279 developed synchronously with layers' tilting, and in particular, as developed at least after layers have become near vertical.
280 The top-to-the hinterland shear sense and the small unconformity angle observed in the northern limb, instead, point out for a
281 small initial unconformity angle.

282   A cautionary note must be added for these conclusions, as they are based on a purely geometric model, in which
283 both bed thickness and line length preserves during folding. However, based on field observation reported here and in Tavani
284 et al (2011), pressure solution cleavage is an extremely localized phenomenon in this anticline, and deformation structures
285 pointing out for folding-related bed thickness variations are not occurring. In agreement, and despite the intrinsic
286 simplification of any geometric model, information provided by the model of figure 6 can be applied to our case study.

287

6. Discussion

6.1 Relative timing between shearing and layers' tilting

290   Strata of the Vallcarga Group exposed at the forelimb of the Sant Corneli-Bóixols Anticline display a rather constant
291 attitude, however, according to the model described in figure 6, shear senses and angles of the unconformity on top of these
292 strata, indicate that the pre-unconformity layers (i.e. the Vallcarga Group) were not homoclinally-dipping when the Areny

293 Group was unconformably deposited on top them. The scheme of Figure 7a illustrates the present day simplified geometry of

294 the studied structure, together with the balanced (i.e. line-length is preserved; Dahlstrom, 1969; Brandes and Tanner, 2014)

295 reconstruction at a time immediately after the unconformity development. The reconstructed dip of pre-unconformity layers

296 in the three limbs, is obtained according to what illustrated in section 5. As previously mentioned, the top-to-the-foreland

297 shearing along the unconformity of the central limb has to be interpreted as occurring when strata of the Vallcarga Group

298 attained a near-vertical to overturned attitude. On the other hand, the absence of any evidence of top-to-the-hinterland

299 shearing along the unconformity surface at the central limb, points out that such an unconformity had to be developed when

300 the layers of the Vallcarga Group were steeply dipping. In agreement with this, the north-dipping faults offsetting the sheared

301 unconformity have to be regarded as syn-folding structures developed when strata of the Vallcarga Group were overturned.

302 These 10- to 30-m spaced faults mostly consist of bedding-parallel segments (Figs. 4A and 5d), with some strands showing

303 cut-off angles between 20° and 40° (see stereoplots of figures 3b-c), and are interpreted as flexural-slip faults, like those

304 offsetting the topographic surface of growth folds (e.g. Burbank and Anderson, 2011; Gutiérrez et al., 2014; Li et al., 2015).

305 These faults are therefore late-stage flexural-slip features and, as detailed in the next sub-section, cannot be compatible with

306 a sub-horizontal maximum stress.

6.2 Maximum stress orientation

308 The studied natural stratigraphic units includes cm to m-thick strata of limestones, marls, sandstones and

309 conglomerates exposed across an about 500-m-wide area (Fig. 1). The large number of strata involved in the deformation,

310 coupled with their high compositional variability, prevents the collection of a representative dataset of friction and cohesion

311 data of both layers and interlayers. It thus makes it impossible to carry out a quantitative dynamic (i.e. stress) reconstruction.

312 However, many stress configurations can be easily discarded, due to their kinematic inconsistency with the observed

313 shearing pattern. In particular, we consider that the maximum paleo-stress lies on the plane oriented perpendicular to the

314 fault/flexural-slip plane and containing the slip direction, and forms an obtuse angle with the shear sense (e.g. Etchecopar et

315 al., 1981). The following observations can thus restrict the range of possible solution and the sources of stress during folding:

316 (1) If we consider faults and strata in their present orientation and after plunge and bedding dip removal, the top-to-the-

317 foreland layer-parallel shearing and the south-verging reverse faulting are rare features in the northern limb of the San

318 Maximí Syncline, which is located at a distance of less than 100 m from the Bóixols thrust. The scarcity of these structures,

319 and the occurrence of flexural-slip surfaces forming a low angle with the thrust and having an opposite shear sense (i.e.

320 normal kinematics), indicates the limited role of faulting-related stress, sourced from the process zone (e.g. Cowie and

321 Scholz, 1992) of the upward propagating Bóixols thrust, in controlling the pattern of syn-folding shearing. This is contrary to

322 what has instead been documented in other thrust-related anticlines (e.g. Bellahsen et al., 2006). (2) The top-to-the-hinterland

323 (i.e. top-to-the-crest of the Sant Corneli-Bóixols Anticline) layer-parallel shearing observed along the bedding surfaces of the

324 Vallcarga Group for all the three limbs has to be regarded as syn-folding. With the exception of few bedding-oblique strands

325 of flexural-slip faults, no significant evidence of strata thinning/thickening has been observed in the Vallcarga group. This

326 points out that, folding has been almost entirely produced by layer parallel-shearing with bed-thickness preservation until
327 late stage flexural-slip faulting took place (e.g. Donath and Parker, 1964). (3) Deformation structures such as the layer-
328 (nearly) parallel shortening related cleavage measured in the silty levels of the Areny Group along the axial zone of the San
329 Maximí syncline indicate a maximum stress oriented at a low angle to bedding (Fig. 2d). (4) The fourth key observation
330 concerns the steeply-dipping faults, with high cutoff angles, cutting and displacing the unconformity. These faults include
331 steps with cut-off angles of about 30° and steps parallel to the overturned bedding surfaces. Under the assumption that late-
332 stage flexural slip faulting caused the arrest of shearing along the unconformity, a range of possible maximum stress
333 orientation during the transition from top-to-the-foreland shearing along the unconformity to the late-stage flexural-slip
334 faulting can be defined for the central limb, as shown in figure 7b. The angle between the maximum stress and the bedding-
335 parallel steps of flexural-slip faults in the Vallcarga Group is α, the angle between the maximum stress and the flexural-slip
336 fault strands oblique to bedding in the Vallcarga Group is β, whereas the angle between the maximum stress and the
337 unconformity is γ. These three angles must be comprised between 0 and 90° to produce the observed shear pattern and for it
338 to be kinematically compatible. When using the average dip of the unconformity (i.e. 0°) and the dip of the Vallcarga Group
339 strata in the central limb (i.e. 60° overturned), a maximum stress dip (labelled $d\sigma_1$ in figure 7d) ranging from 30° to 90° is
340 obtained.

341   At this stage one may argue that the maximum stress was inclined only during the latest stage of folding, when pre-
342 kinematic strata were overturned, while the maximum stress was sub-horizontal during most of the folding process. Such a
343 scenario, in which the reorientation of the maximum stress is a discontinuous process, contrasts with the fact that, in order to
344 produce shearing along bedding surfaces, the maximum stress should have been south-dipping not only when strata were 60°
345 overturned. In fact, dip-slip shearing along upright layers also requires the maximum stress to be south-dipping, and such a
346 stress configuration can be extrapolated also for steeply (e.g. >75°) south-dipping strata. In agreement, it is intuitive the
347 conclusion that the stress rotation was not a discontinuous process, but instead it has continuously operated during folding.

348   As documented in Tavani et al (2011), the layer parallel shortening pattern in the the Sant Corneli-Bóixols Anticline
349 indicates a sub-horizontal maximum stress before folding and during the early stages of folding. As evidenced by data
350 presented here, the stress was in a configuration not allowing shearing (referring to faulting in the Vallcarga layers) during
351 almost the entire folding process. Such stress configuration was able to produce shearing along the bedding surfaces and
352 along the unconformity, with faulting in the Vallcarga and Areny groups being almost negligible. Apart from those structures
353 associated with the layer-parallel shearing, the few additional deformation structures point out for a maximum stress oriented
354 at low angle to bedding. During the late stage of folding instead, when the unconformity angle exceeded 120-130°, the
355 maximum stress was south-dipping, with an angle higher than 30°. The stress attained a state allowing shearing, as faulting
356 in the Vallcarga started. Contextually, bedding surfaces of the Vallcarga continued to be sheared, while shearing along the
357 unconformity (in the central limb) arrested.

6.3 Flexural-slipping and stress reorientation

The information discussed above evidences for a syn-folding maximum stress rotation/reorientation within the growing anticline, from sub-horizontal early-folding layer-parallel shortening in Tavani et al (2011) to south-dipping maximum stress in overturned strata documented here. As schematically illustrated in figure 7d, we infer that the sub-horizontal maximum stress applied to the leading syncline of the growing Sant Corneli-Bóixols Anticline (i.e. the remote applied stress has an andersonian compressive configuration; Anderson, 1951), progressively rotated as it was transmitted across folding rock volumes affected by widespread flexural-slipping. In agreement with what illustrated in the introduction, here this process of stress deflection is interpreted as associable with the flexural-slipping mechanism. In fact, as largely documented, shearing along low-friction faults produces the perturbation of the remotely applied stress field (e.g. Pollard and Segall, 1987; Soliva et al., 2010) and, in particular, reduction of the fault-parallel shear stress component causes the orientation of principal stress to rotate locally towards a fault-parallel direction. Consistently with this, the coupling between flexural-slip and maximum stress reorientation documented in other structures, has been attributed to the fact that slipping along closely spaced low friction bedding surface imposes the maximum stress to orient at low angle to the slipping bedding surface in a wide area (i.e. the flexural-slip folded area), as mentioned in the introduction (Wiltschko et al., 1985; Ohlmacher and Aydin, 1997; Tavani et al. 2012). This concept fully applies to the data presented in this work until the strata attained a strongly overturned attitude.

7 Conclusions

The key questions in this study were to constrain up to the range of dip values over which the flexural slip mechanism can operate.. This fundamental information allows to discriminate whether flexural-slipping is a nearly passive process with respect to the stress field evolution (i.e. the remotely applied stress is only locally deflected) or rather, it is a fully active process, discontinuous at the local scale but sufficiently dense in time and space at the scale of the fold, able to reorient the remotely applied stress field. The answer is that flexural-slip in the studied structures was an active process. It operated up to 120° of dip and caused the maximum stress to progressively reorient at low angle to bedding until strata attained an overturned attitude.

Solid Earth
Discussions

Open Access

EGU

391 **References**

392 Alonso, J.L., 1989. Fold reactivation involving angular unconformable sequences: theoretical analysis and natural examples

393 from the Cantabrian Zone (Northwest Spain). Tectonophysics, 170, 57-77.

394 Anderson E.M., 1951. The Dynamics of Faulting. Oliver and Boyd, Edinburgh.

395 Arbués, P., Pi, E., Berástegui, X., 1996. Relaciones entre la evolución sedimentaria del Grupo de Arén y el cabalgamiento de

396 Bóixols (Campaniense terminal-Maastrichtiense del Pirineo meridional-central). Geogaceta, 20, 446-449.

397 Balsamo, F., Clemenzi, L., Storti, F., Mozafari, M., Solum, J., Swennen, R., Taberner, C., Tueckmantel, C. 2016. Anatomy

398 and paleofluid evolution of laterally restricted extensional fault zones in the Jabal Qusaybah anticline, Salakh arch,

399 Oman. Geological Society of America Bulletin, 128(5-6), 957-972.

400 Beamud, E., Muñoz, J.A., Fitzgeral, P.G., Baldwin, S.L., Garcés, M., Cabrera, L., Metcalf, J.R., 2011. Magnetostratigraphy

401 and detrital apatite fission track thermochronology in syntectonic conglomerates: constraints on the exhumation of the

402 South-Central Pyrenees. Basin Research 23, 309-331.

403 Beaudoin, N., Leprêtre, R., Bellahsen, N., Lacombe, O., Amrouch, K., Callot, J.P., Emmanuel, L., Daniel, J.M., 2012.

404 Structural and microstructural evolution of the Rattlesnake Mountain Anticline (Wyoming, USA): new insights into the

405 Sevier and Laramide orogenic stress build-up in the Bighorn Basin. Tectonophysics 576, 20-45.

406 Belayneh, M., Cosgrove, J.W., 2004. Fracture-pattern variations around a major fold and their implications regarding

407 fracture prediction using limited data: an example from the Bristol Channel Basin. Geological Society, London, Special

408 Publications, 231, 89-102.

409 Bellahsen, N., Fiore, P.E., Pollard, D.D., 2006. From spatial variation of fracture patterns to fold kinematics: A

410 geomechanical approach. Geophysical Research Letters, 33, L02301

411 Berástegui, X., García-Senz, J.M., Losantos, M., 1990. Tecto-sedimentary evolution of the Organya extensional basin

412 (central south Pyrenean unit, Spain) during the Lower Cretaceous. Bulletin de la Societe Geologique de France, 8, 251-264.

413 Bond, R.M.G., McClay, K.R., 1995. Inversion of a Lower Cretaceous extensional basin, south central Pyrenees, Spain.

414 Geological Society, London, Special Publications, 88, 415-431.

415 Brandes, C., Tanner, D.C., 2014. Fault-related folding: A review of kinematic models and their application. Earth-Science

416 Reviews, 138, 352-370.

417 Burbank, D., Meigs, A., Brozović, N., 1996. Interactions of growing folds and coeval depositional systems. Basin Research,

418 8, 199-223.

419 Burbank, D.W., Anderson, R.S., 2011. Tectonic geomorphology. Blackwell, Oxford.

420 Callot, J.P., Robion, P., Sassi, W., Guiton, M.L.E., Faure, J.-L., Daniel, J.M., Mengus, J.-M., Schmitz, J., 2010. Magnetic

421 characterisation of folded aeolian sandstones: Interpretation of magnetic fabrics in diamagnetic rocks. Tectonophysics, 495,

422 230-245.

423 Choukroune, P., Roure, F., Pinet, B., 1990. Main results of the ECORS Pyrenees profile. Tectonophysics, 173, 411-423

424 Cowie, P.A., Scholz, C.H., 1992. Displacement-length scaling relationship for faults: data synthesis and discussion. Journal

13

425   of Structural Geology, 14, 1149-1156.

426   Cuevas, J.L., 1992. Estratigrafía del" Garumniense" de la Conca de Tremp. Prepirineo de Lérida. Acta geológica hispánica,
427   27, 95-108.

428   Dahlstrom, C.D.A., 1969. Balanced cross sections. Can. J. Earth Sci. 6, 743-757.

429   Donath, F.A., Parker, R.B., 1964. Folds and folding. Geol. Soc. Am. Bull., 75, 45-62.

430   Etchecopar, A., Vasseur, G., Daignieres, M., 1981. An inverse problem in microtectonics for the determination of stress
431   tensors from fault striation analysis. Journal of Structural Geology, 3, 51-65.

432   Engelder, T., Geiser, P., 1980. On the use of regional joint sets as trajectories of paleostress fields during the development of
433   the Appalachian plateau, New York. Journal of Geophysical Research, 85, 6319-6341.

434   Erslev, E.A., Mayborn, K.R., 1997. Multiple geometries and modes of fault-propagation folding in the Canadian thrust belt.
435   J. Struct. Geol., 19, 321-335.

436   Fischer, M.P., Wilkerson, M.S., 2000. Predicting the orientation of joints from fold shape: results of pseudo-three-
437   dimensional modeling and curvature analysis. Geology 28, 15-18.

438   Ford, M., Williams, E. A., Artoni, A., Vergés, J., Hardy, S., 1997. Progressive evolution of a fault-related fold pair from
439   growth strata geometries, Sant Llorenç de Morunys, SE Pyrenees. Journal of structural Geology, 19, 413-441.

440   Fowler, T.J., 1996. Flexural-slip generated bedding-parallel veins from central Victoria, Australia. Journal of Structural
441   Geology, 18, 1399-1415.

442   García-Senz, J., 2002. Cuencas extensivas del Cretácico Inferior en los Pirineos centrales. Formación y subsecuente
443   inversión. PhD Thesis, pp. 310. Universitat de Barcelona.

444   Garrido, A., 1973. Estudio geologico y relacion entre teclonica y sedimentacion del Secundario y Terciario de la vertiente
445   meridional Pirenaica en su zona central. PhD Thesis, pp. 395, Universidad de Granada.

446   Gutiérrez, F., Carbonel, D., Kirkham, R. M., Guerrero, J., Lucha, P., Matthews, V. 2014. Can flexural-slip faults related to
447   evaporite dissolution generate hazardous earthquakes? The case of the Grand Hogback monocline of west-central Colorado.
448   Geological Society of America Bulletin, 126, 1481-1494.

449   Hancock, P.L., 1985. Brittle microtectonics: principles and practice. Journal of Structural Geology, 7, 437-457.

450   Lacombe, O., 2012. Do fault slip data inversions actually yield "paleostresses" that can be compared with contemporary
451   stresses? A critical discussion. Comptes Rendus Geoscience, 344, 159-173.

452   Laubach, S.E., 1989. Paleostress directions from the preferred orientation of closed microfractures (fluid-inclusion planes) in
453   sandstone, East Texas basin, U.S.A., Journal of Structural Geology, 11, 15, 603-611.

454   Lanaja, J.M., 1987. Contribución de la exploración petrolífera al conocimiento de la geología de España. pp. 465. IGME,
455   Madrid.

456   Li, T., Chen, J., Thompson, J. A., Burbank, D. W., Yang, X., 2015. Active flexural-slip faulting: A study from the Pamir-Tian
457   Shan convergent zone, NW China. Journal of Geophysical Research: Solid Earth, 120, 4359-4378.

458   Lisle, R.J., 1994. Detection of zones of abnormal strains in structures using Gaussian curvature analysis. AAPG Bull., 78,

459   1811-1819.

460   Medwedeff, D.W., 1989. Growth fault-bend folding at southeast Lost Hills, San Joaquin Valley, California. Bulletin of the

461   American Association of Petroleum Geologists, 73, 54-67

462   Mencos, J., 2011. Metodologies de reconstrucció i modetització 3D d'estructures geològiques: anticlinal de Sant Corneli-

463   Bóixols (Pirineus centrals). PhD Thesis, pp. 277. Universitat de Barcelona.

464   Mencos, J., Carrera, N., Muñoz, J.A., 2015. Influence of rift basin geometry on the subsequent postrift sedimentation and

465   basin inversion: The Organyà Basin and the Bóixols thrust sheet (south central Pyrenees). Tectonics, 34, 1452-1474

466   Mitra, S., 1990. Fault-propagation folds: geometry, kinematic evolution, and hydrocarbon traps. AAPG Bull. 74, 921-945.

467   Muñoz, J.A., 1992. Evolution of a continental collision belt: ECORS-Pyrenees crustal balanced cross-section. In *Thrust*

468   *tectonics*, K.R. McClay ed., pp. 235-246, Chapman & Hall, London.

469   Muñoz, J.A., 2002. The Pyrenees. In *The Geology of Spain*, W. Gibbons and T. Moreno eds., 370-385, Geological Society,

470   London.

471   Muñoz, J.A., Carrera, N., Mencos, J., Beamud, B., Perea, H., Arbués, P., Rivas, G., Bausà J., Garcia-Senz, J., 2010.

472   *Cartografia geològica del substrat prequaternari*. Map 252-2-2 (66–22), Aramunt scale 1: 25000, Institut Cartogràfic de

473   Catalunya (ICC), Servei Geològic de Catalunya (IGC), Barcelona.

474   Nagtegaal, P.J.C., 1972. Depositional history and clay minerals of the Upper Cretaceous basin in the South-Central Pyrenees,

475   Spain. Leidse Geologische Mededelingen, 47, 251-275.

476   Nicol, A., Nathan, S., 2001. Folding and the formation of bedding-parallel faults on the western limb of Grey Valley

477   Syncline near Blackball, New Zealand. New Zealand Journal of Geology and Geophysics, 44, 127-135.

478   Ohlmacher, G.C., Aydin, A., 1997. Mechanics of vein, fault and solution surface formation in the Appalachian Valley and

479   Ridge, northeastern Tennessee, USA: implications for fault friction, state of stress and fluid pressure. J. Struct. Geol. 19,

480   927–944.

481   Poblet, J., Storti, F., McClay, K., Muñoz, J.A., 1997. Geometries of syntectonic sediments associated with single-layer

482   detachment folds. Journal of Structural Geology, 19, 369-381.

483   Pollard, D.D., Segall, P., 1987. Theoretical displacements and stresses near fractures in rock: with applications to faults,

484   joints, veins, dikes, and solution surfaces. Fracture mechanics of rock. Academic Press. London

485   Price, N.J., Cosgrove, J.W., 1990. Analysis of Geological Structures.

486   Ramsay, J.G., 1967. Folding and Fracturing of Rocks. McGraw-Hill, New York.

487   Roma, M., Arbués, P., Granado, P., Gratacós, O., Muñoz, J.A., 2011. The Sallent growth strata: an example of complex fold

488   amplification mechanisms interacting with deepwater to continental sedimentation (South-Central Pyrenees, Spain).

489   Abstracts with Poster, T4b. Sedimentation and Tectonics, 28th IAS Meeting of Sedimentology 2011

490   Rosell, J., 1963. Sobre la existencia de la discordancia precenomaniense en el Pirineo de la provincia de Lerida. Notas y

491   Comunicaciones del Instituto Geológico y Minero de España, 72, 71-80.

492   Shackleton, J.R., Cooke, M.L., Sussman, A.J., 2005. Evidence for temporally changing mechanical stratigraphy and effects

493   on joint-network architecture. Geology, 33, 101-104.

494   Shackleton, J.R., Cooke, M.L., Vergés, J., Simó, T., 2011. Temporal constraints on fracturing associated with fault-related

495   folding at Sant Corneli anticline, Spanish Pyrenees. Journal of Structural Geology, 33, 5-19.

496   Simó, A. 1986. Carbonate platform depositional sequences, Upper Cretaceous, South Central Pyrenees (Spain).

497   Tectonophysics, 129, 205-231.

498   Soliva, R., Maerten, F., Petit, J. P., Auzias, V., 2010. Field evidences for the role of static friction on fracture orientation in

499   extensional relays along strike-slip faults: Comparison with photoelasticity and 3-D numerical modeling. Journal of

500   Structural Geology, 32, 1721-1731.

501   Suppe, J., 1983. Geometry and kinematics of fault–bend folding. American Journal of Science, 283, 684-721.

502   Suppe, J., Medwedeff, D.A., 1990. Geometry and kinematics of fault-propagation folding. Eclogae Geol. Helv. 83, 409-454.

503   Suppe, J., Chou, G.T., Hook, S.C., 1992. Rates of folding and faulting determined from growth strata. In *Thrust tectonics*,

504   K.R. McClay ed., pp. 105-121. Chapman & Hall, London.

505   Suppe, J., Sàbat, F., Muñoz, J. A., Poblet, J., Roca, E., Vergés, J., 1997. Bed-by-bed fold growth by kink-band migration:

506   Sant Llorenç de Morunys, eastern Pyrenees. Journal of Structural Geology, 19, 443-461.

507   Tanner, P.W., 1989. The flexural-slip mechanism. Journal of Structural Geology. 11, 635-655.

508   Tavani, S., Storti, F., Fernández, O., Muñoz, J.A., Salvini, F., 2006. 3-D deformation pattern analysis and evolution of the

509   Anisclo anticline, southern Pyrenees. Journal of Structural Geology, 28, 695-712.

510   Tavani, S., Mencos, J., Bausà, J., Muñoz, J.A., 2011. The fracture pattern of the Sant Corneli Bóixols oblique inversion

511   anticline (Spanish Pyrenees). Journal of Structural Geology, 33, 1662-1680.

512   Tavani, S., Storti, F., Bausà, J., Muñoz, J.A., 2012. Late thrusting extensional collapse at the mountain front of the northern

513   Apennines (Italy). Tectonics, 31 (4), TC4019.

514   Tavani, S., Storti, F., Lacombe, O., Corradetti, A., Muñoz, J. A., Mazzoli, S., 2015. A review of deformation pattern

515   templates in foreland basin systems and fold-and-thrust belts: Implications for the state of stress in the frontal regions of

516   thrust wedges. Earth-Science Reviews, 141, 82-104.

517   Teixell, A., 1998. Crustal structure and orogenic material budget in the west central Pyrenees. Tectonics, 17, 395-406.

518   Tesei, T., Collettini, C., Vitic, C., Barchi, M.R., 2013. Fault architecture and deformation mechanisms in exhumed analogues

519   of seismogenic carbonate-bearing thrusts. Journal of Structural Geology, 55, 167–181

520   Tugend, J., Manatschal, G., Kusznir, N. J., Masini, E., Mohn, G., Thinon, I., 2014. Formation and deformation of

521   hyperextended rift systems: Insights from rift domain mapping in the Bay of Biscay-Pyrenees. Tectonics, 33(7), 1239-1276.

522   Vergés, J., Fernàndez, M., Martínez, A., 2002. The Pyrenean orogen: pre-, syn-, and post-collisional evolution. Journal of the

523   Virtual Explorer, 8, 57-76.

524   Wiltschko, D.V., Medwedeff, D.A., Millson, H.E., 1985. Distribution and mechanisms of strain within rocks on the

525   northwest ramp of Pine Mountain block, southern Appalachian foreland: a field test of theory. Geological Society of America

526   Bulletin, 96, 426-435.

Solid Earth
Discussions

Open Access

EGU

527 Vitale, S., Zaghloul, M.N., Tramparulo, F.D.A, El Ouaragli, B., 2014. Deformation characterization of a regional thrust zone

528 in the northernRif (Chefchaouen, Morocco). Journal of Geodynamics, 77, 22-38

529 Zapata, T.R., Allmendinger, R.W., 1996. Growth stratal records of instantaneous and progressive limb rotation in the

530 Precordillera thrust belt and Bermejo basin, Argentina. Tectonics, 15, 1065-1083

531 **Captions**

532 **Figure 1**: (A) Geological maps of eastern Pyrenees, with detail of the Sant Corneli-Bóixols Anticline. Geological map (B) and schematic

533 cross-section (C) of the study area, with cumulative contouring of poles to bedding and best-fit beta axis. (D) Panoramic view of the study

534 area, with insets showing the location of figures 2 to 4 and the photographed area in cross-section and map-view, respectively.

535 **Figure 2**: Structures exposed at the northern limb of the San Maximí Syncline. (A) Cross-sectional location of the site. (B) South-dipping

536 conglomerates of the Areny Group unconformably overlying the overturned north-dipping strata of the Vallcarga Group, with stereoplots

537 of the unconformity and bedding surfaces in the Vallcarga Group. (C) Detail of the unconformity, showing S-C-C' fabric, with

538 corresponding stereoplots. (D) South-dipping alternating conglomerates and siltstones of the Areny Group, with pervasive cleavage at high

539 angle to bedding.

540 **Figure 3:** Transitional area between the San Maximí Syncline and the Remolina Anticline. (A) Cross-sectional location of the site. (B)

541 Shallow-dipping unconformity between the Areny and the Vallcarga groups reactivated as a low-angle fault and displaced by a high-angle

542 fault. Details of the low- and high-dipping faults are shown, together with stereoplots of faults and bedding surfaces of the Vallcarga

543 Group. (C) Panoramic view and stereoplot of a near vertical fault system uplifting the Remolina Anticline, which has folded strata of the

544 Areny Group unconformably on top of near vertical strata of the Vallcarga Group.

545 **Figure 4:** Macro- and meso-structures of the Remolina Anticline. (A) Panoramic view and line-drawing of the Remolina Anticline (with

546 insets showing the location of figure 4B and C, and figure 5B), with stereoplots of faults and bedding measured in the Vallcarga Group. (B)

547 Detail of a south-dipping reverse fault having in its footwall sub-horizontal carbonates of the Areny Group on top of overturned strata of

548 the Vallcarga Group. Stereoplots show fault data in the Areny carbonates. (C) Details of the unconformity, with S-C-C' illustrated and

549 plotted.

550 **Figure 5:** (A) Panoramic view of the hinge zone of the Remolina anticline, visible in the Areny strata that are on top of constantly-dipping

551 strata of the Vallcarga Group. (B) Detail of the unconformity between Areny and Vallcarga groups at the southern limb of the anticline,

552 where no evidence of shear occurs. (C) Detail of slickenlines along a near vertical bedding surface of the Areny strata, providing a top to

553 the north shear sense for the upper bed. (D) Stereoplots of bedding surfaces and faults collected in the Areny Group strata of the southern

554 limb of the Remolina Anticline.

555 **Figure 6:** (A) Evolving angular relationships between unconformable sequences during flexural-folding in the inner limb of a syncline,

556 with shear senses along pre-unconformity layers and along the unconformity indicated, for different initial unconformity angles. The

557 position of six key-points undergoing folding is illustrated, as well as the dip of pre-unconformity layers (D) and of the unconformity angle

558 (U), which is the angle between the unconformity and the underlying layers. (B) X and Y coordinates of the six points of figure 6a, with

559 length of segments, and derived amount of shear along the unconformity (ΔS) and unconformity angle (U). (C) Graphical solution of

560 equations in figure 6b. Blue lines relate the unconformity angle (U) to the dip of pre growth strata (D) for different initial unconformity

561 angle (U_0). Red lines relates the normalised shear along the unconformity in the inner portion (i.e. $\Delta S = P_4P_5$ segment divided H) to D, for

562 different initial unconformity angle (U_0). Notice that the Y axis for red lines is on the right and that positive and negative values are

563 flipped. The lines indicate the cumulative shear along the unconformity, while the grey area bordered by the black line, indicate the area

564 where the incremental shear is negative.

565 **Figure 7:** (A) Scheme showing the present day geometry of the frontal limb of the Sant Corneli-Bóixols Anticline. (B) Details showing the

566 structural assemblages observed at the Remolina Anticline, with two alternative configurations for the maximum stress orientation. The

567 maximum stress forms the following clockwise angles: $d\sigma_1$ with the horizontal, γ with the unconformity, α with the bedding-parallel steps

568 of flexural-slip faults in the Vallcarga Group, β with the oblique to bedding strands of the flexural-slip fault in the Vallcarga Group. Red

569 and cyan colours indicate angles not compatible and compatible with the observed shear pattern, respectively. (C) Relationships between

570 $d\sigma_1$, and α, β, and γ, with the red area indicating the orientation of the maximum stress not compatible with the shear pattern observed at

571 the Remolina Anticline. (D) Inferred maximum stress trajectories during the late stages of folding.
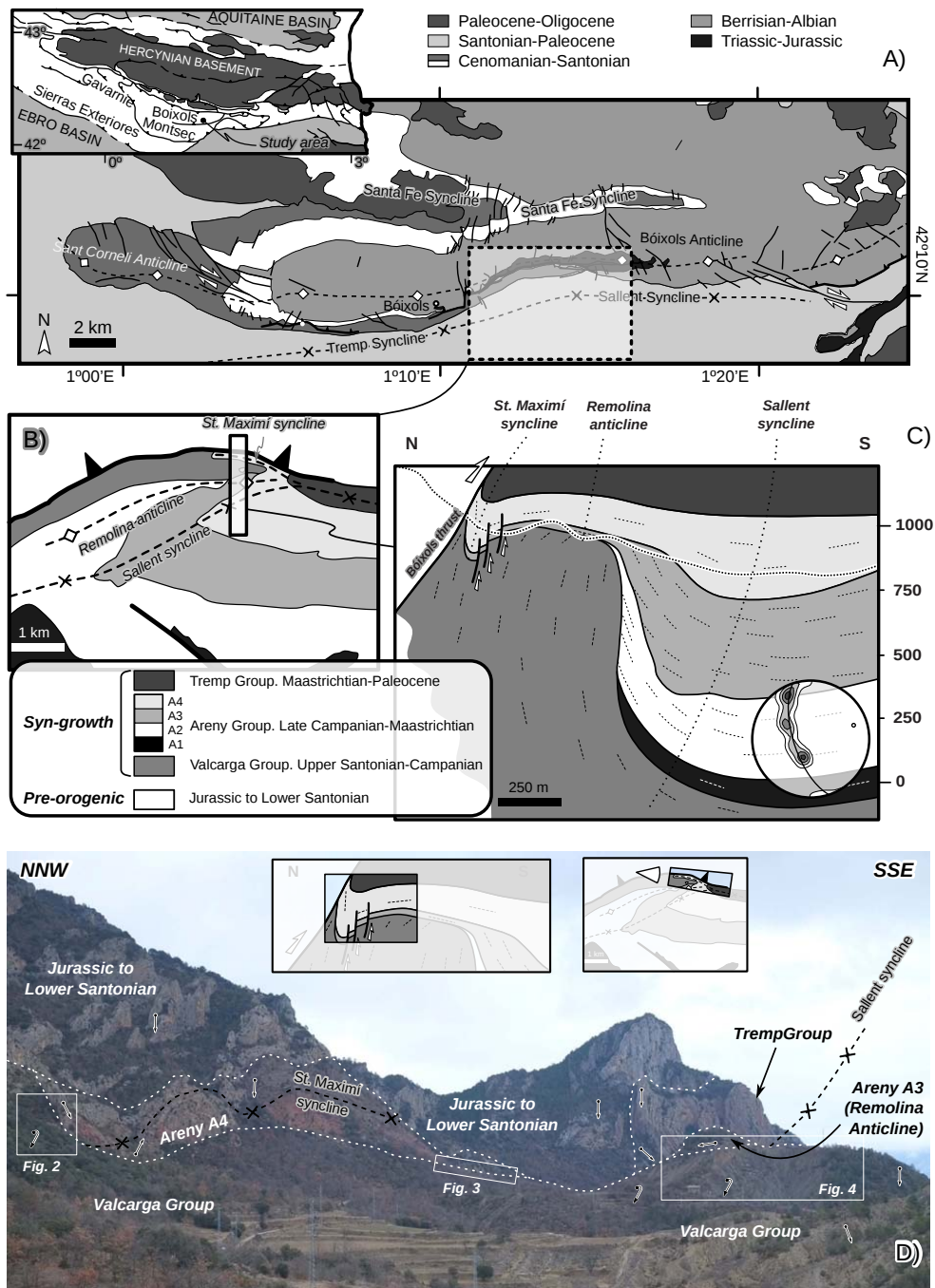
Figure 1: (A) Geological maps of eastern Pyrenees, with detail of the Sant Corneli-Bóixols Anticline. Geological map (B) and schematic cross-section (C) of the study area, with cumulative contouring of poles to bedding and best-fit beta axis. (D) Panoramic view of the study area, with insets showing the location of figures 2 to 4 and the photographed area in cross-section and map-view, respectively.
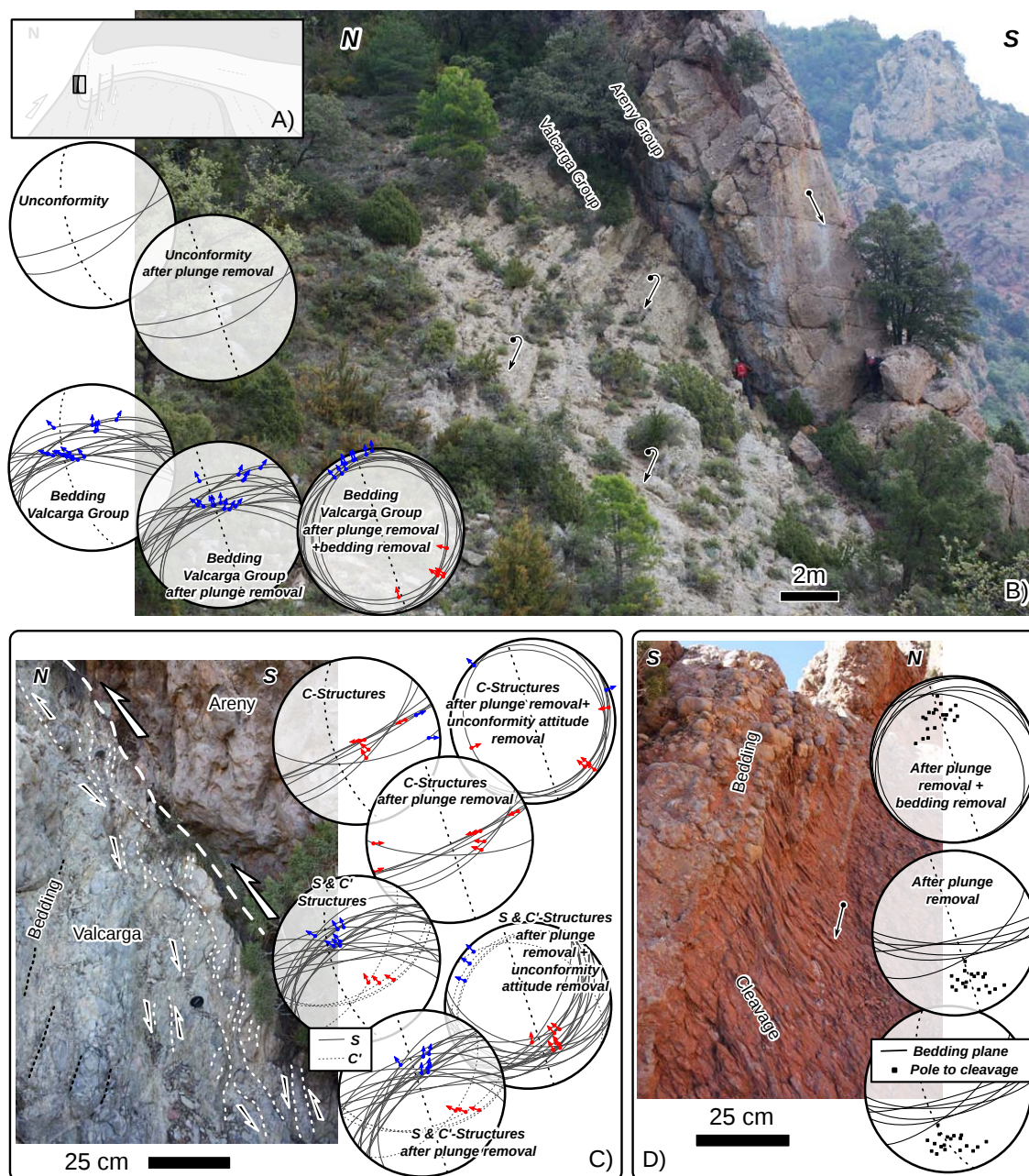
Figure 2: Structures exposed at the northern limb of the San Maximí Syncline. (A) Cross-sectional location of the site. (B) South-dipping conglomerates of the Areny Group unconformably overlying the overturned north-dipping strata of the Vallcarga Group, with stereoplots of the unconformity and bedding surfaces in the Vallcarga Group. (C) Detail of the unconformity, showing S-C-C' fabric, with corresponding stereoplots. (D) South-dipping alternating conglomerates and siltstones of the Areny Group, with pervasive cleavage at high angle to bedding.
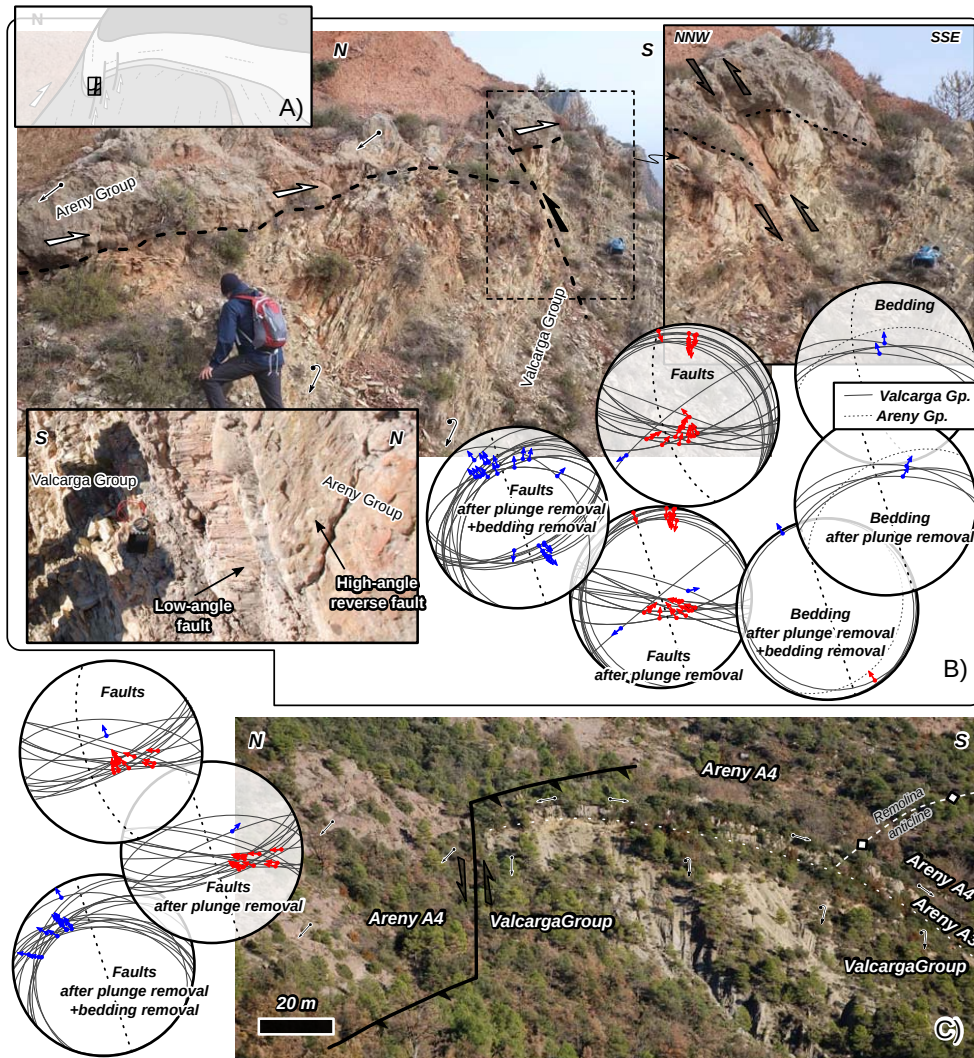
Figure 3: Transitional area between the San Maximí Syncline and the Remolina Anticline. (A) Cross-sectional location of the site. (B) Shallow-dipping unconformity between the Areny and the Vallcarga groups reactivated as a low-angle fault and displaced by a high-angle fault. Details of the low- and high-dipping faults are shown, together with stereoplots of faults and bedding surfaces of the Vallcarga Group. (C) Panoramic view and stereoplot of a near vertical fault system uplifting the Remolina Anticline, which has folded strata of the Areny Group unconformably on top of near vertical strata of the Vallcarga Group.
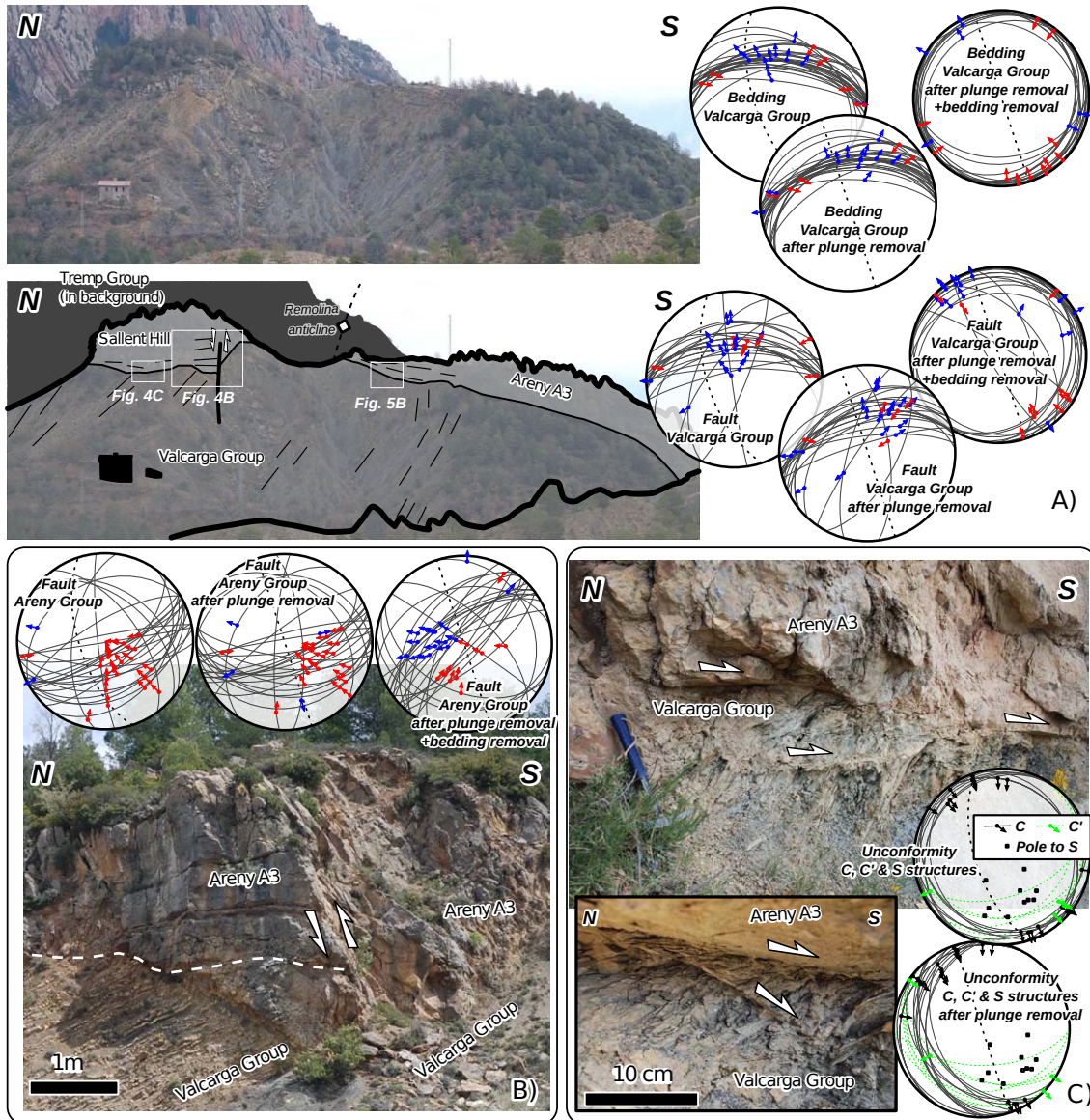
Figure 4: Macro- and meso-structures of the Remolina Anticline. (A) Panoramic view and line-drawing of the Remolina Anticline (with insets showing the location of figure 4B and C, and figure 5B), with stereoplots of faults and bedding measured in the Vallcarga Group. (B) Detail of a south-dipping reverse fault having in its footwall sub-horizontal carbonates of the Areny Group on top of overturned strata of the Vallcarga Group. Stereoplots show fault data in the Areny carbonates. (C) Details of the unconformity, with S-C-C' illustrated and plotted.
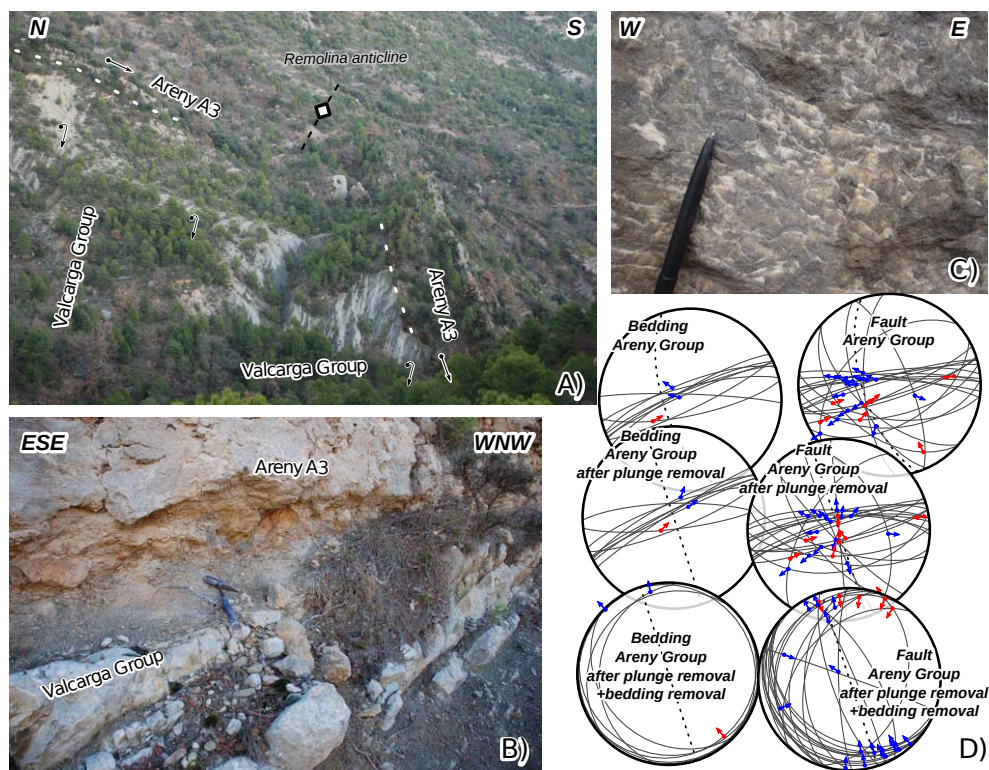
Figure 5: (A) Panoramic view of the hinge zone of the Remolina anticline, visible in the Areny strata that are on top of constantly-dipping strata of the Vallcarga Group. (B) Detail of the unconformity between Areny and Vallcarga groups at the southern limb of the anticline, where no evidence of shear occurs. (C) Detail of slickenlines along a near vertical bedding surface of the Areny strata, providing a top to the north shear sense for the upper bed. (D) Stereoplots of bedding surfaces and faults collected in the Areny Group strata of the southern limb of the Remolina Anticline.
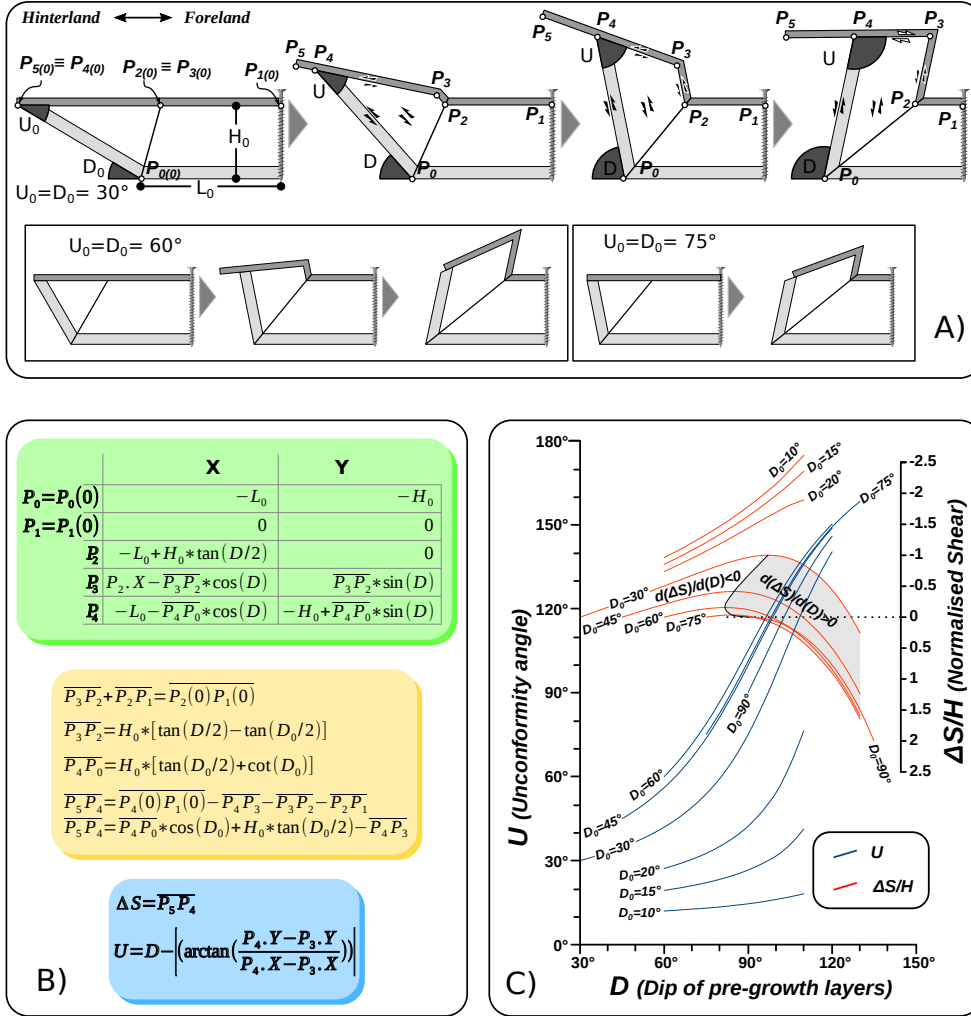
Figure 6: (A) Evolving angular relationships between unconformable sequences during flexural-folding in the inner limb of a syncline, with shear senses along pre-unconformity layers and along the unconformity indicated, for different initial unconformity angles. The position of six key-points undergoing folding is illustrated, as well as the dip of pre-unconformity layers (D) and of the unconformity angle (U), which is the angle between the unconformity and the underlying layers. (B) X and Y coordinates of the six points of figure 6a, with length of segments, and derived amount of shear along the unconformity (ΔS) and unconformity angle (U). (C) Graphical solution of equations in figure 6b. Blue lines relate the unconformity angle (U) to the dip of pre growth strata (D) for different initial unconformity angle (U0). Red lines relates the normalised shear along the unconformity in the inner portion (i.e. ΔS = P4P5 segment divided H) to D, for different initial unconformity angle (U0). Notice that the Y axis for red lines is on the right and that positive and negative values are flipped. The lines indicate the cumulative shear along the unconformity, while the grey area bordered by the black line, indicate the area where the incremental shear is negative.
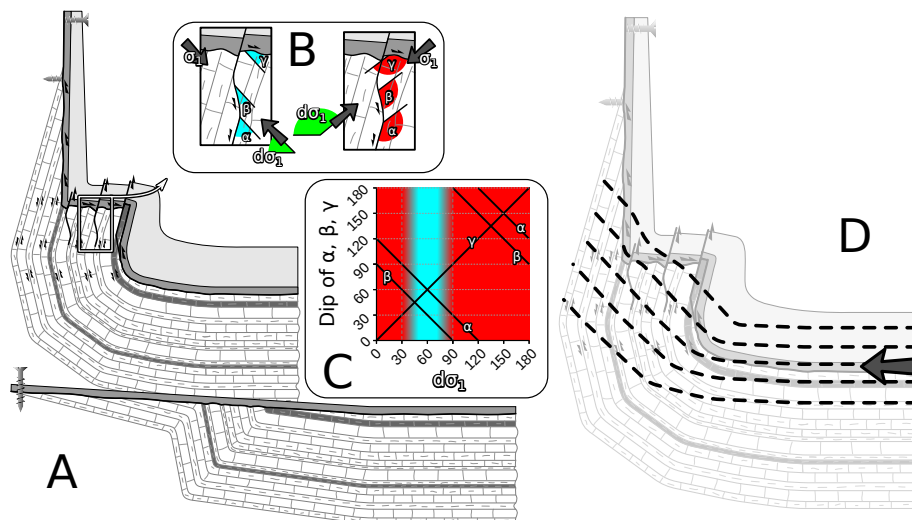
Figure 7: (A) Scheme showing the present day geometry of the frontal limb of the Sant Corneli-Bóixols Anticline. (B) Details showing the structural assemblages observed at the Remolina Anticline, with two alternative configurations for the maximum stress orientation. The maximum stress forms the following clockwise: $d\sigma_1$ with the horizontal, λ with the unconformity, α with the bedding-parallel steps of flexural-slip faults in the Vallcarga Group, β with the oblique to bedding strands of the flexural-slip fault in the Vallcarga Group. Red and cyan colours indicate angles not compatible and compatible with the observed shear pattern, respectively. (C) Relationships between $d\sigma_1$, and α, β, and λ, with the red area indicating the orientation of the maximum stress not compatible with the shear pattern observed at the Remolina Anticline. (D) Inferred maximum stress trajectories during the late stages of folding.